

# Bistable origami thermal switch with high switching ratios

Received: 28 July 2025

Accepted: 13 February 2026

Published online: 25 February 2026

Bowen Tan<sup>1,2,6</sup>, Jun Lyu<sup>1,6</sup>, Fuwei Yang<sup>3</sup>, Ke Xu<sup>1</sup>, Shuo Qiao<sup>1</sup>, Bai Song<sup>4,5</sup>, Lin Yang<sup>1,5</sup>✉ & Ke Liu<sup>1</sup>✉

Effective thermal management is critical for power electronics in AI and robotics, highlighting the need for dynamic, reversible thermal switches. Achieving a high switching ratio remains challenging. Here, we present a bistable origami-inspired thermal switch that switch rapidly between distinct thermal conduction states without external energy or sensory input. Fabricated from a thin film through precise cut-and-fold, it achieves thermal switching ratios of 13,984 in vacuum and 1360 in ambient air, significantly higher than existing approaches. Switching is driven by snap-through instability, actuated by a combination of shape-memory alloy and elastic springs. The energy landscape can be tuned through geometric variations to adjust triggering temperature and switching ratio. We demonstrate stable, repeatable thermal regulation across multiple scenarios, offering a pathway toward passive, programmable thermal management.

Modulating heat flow with precision-akin to electronic analogs—has been a long-standing aspiration in thermodynamic engineering, which holds the promise of advancing technologies ranging from phononic logic circuits to functional thermal devices<sup>1,2</sup>. However, achieving active and reversible control of thermal conduction (*i.e.*, thermal switch) remains a formidable challenge due to the difficulty of simultaneously meeting essential criteria, including high switching ratio, robust cyclic reliability, passive operation, and bistable functionality. Advances in nanotechnology have extended our understanding of heat carrier transport and enabled innovative approaches to its manipulation<sup>3–6</sup>. Over the past decades, significant efforts have been dedicated to tuning room-temperature thermal transport in solids through temperature/light triggered phase transitions<sup>7,8</sup>, electrochemical scattering motion of ions<sup>9,10</sup>, or electrical/magnetic field-driven structural modulation<sup>11,12</sup>. While these strategies have shown promise, they suffer from critical limitations: low switching ratios (<13)<sup>7–12</sup>, severe performance degradation after limited cycles<sup>9,10</sup>, and the need for continuous external energy input<sup>11,12</sup>, complicating system design and reducing energy efficiency.

An alternative approach involves thermal switches based on the opening and closing of a macroscopic interface. This strategy typically leverages differential thermal expansion between materials to induce geometric changes, exploiting the strongly non-linear behavior of thermal conductance as interfacial gaps close<sup>13,14</sup>. Through developing a shape memory alloy (SMA) actuation configuration to close an interfacial gap, a switching ratio of ~40 in air is achieved, which boosts to ~2000 under vacuum by eliminating natural convection<sup>15</sup>. However, the switching ratio is still impractical under ambient environment. More importantly, thermal switching strategies developed to date (both nanoscale structural engineering and macroscopic gap closing) fail to address a critical gap: the lack of bistable operation. Bistable functionality, essential for binary representation (0 and 1) akin to digital electronics, ensures clear state differentiation, resistance to external perturbations, and threshold-based switching for reliable operation even in noisy environments.

To address the aforementioned challenges, we seek solutions from origami, the ancient art of paper folding<sup>16,17</sup>. In recent years, origami has significantly influenced science and engineering, impacting various fields including condensed matter physics<sup>18</sup>, material

<sup>1</sup>School of Advanced Manufacturing and Robotics, Peking University, Beijing, China. <sup>2</sup>School of Future Technology, Shandong University, Jinan, China.<sup>3</sup>Department of Engineering Mechanics, Tsinghua University, Beijing, China. <sup>4</sup>School of Mechanics and Engineering Science, Peking University, Beijing, China.<sup>5</sup>National Key Laboratory of Advanced Micro and Nano Manufacture Technology, Peking University, Beijing, China. <sup>6</sup>These authors contributed equally: Bowen Tan, Jun Lyu. ✉e-mail: [linyangpku@pku.edu.cn](mailto:linyangpku@pku.edu.cn); [liuke@pku.edu.cn](mailto:liuke@pku.edu.cn)

science<sup>19–22</sup>, mechanical engineering<sup>23–29</sup>, robotics<sup>30–33</sup>, biomedical engineering<sup>34,35</sup>, and architecture<sup>36,37</sup>. At its core, origami transforms flat two-dimensional materials into intricate three-dimensional structures through precise cuts and folds. In particular, by leveraging carefully engineered crease patterns<sup>38–40</sup>, origami leads to bistable structures that can reliably switch between two geometric configurations with distinct thermal conductance. These bistable systems exhibit remarkable mechanical properties, enabling them to snap rapidly from one state to another with programmable energy input<sup>41–43</sup>.

Leveraging the inherent bistability of origami, we introduce a novel passive thermal switch with unprecedented switching ratio. For instance, the passive switch can be applied to a power supply array, allowing pixelated regulation of the temperature of each individual battery (Fig. 1a). Specifically, our design utilizes a bistable origami architecture that enables rapid, reversible switching between two drastically different thermal conduction states, leading to ultrahigh switching ratio (Fig. 1b). The origami structure undergoes flat-state actuation, during which the upper plate remains parallel to the base, such that intimate contact is maintained with either the device or the heat sink. The state switching energy is provided by innovative thermal actuators, which take advantage of the thermal responsiveness of SMA and the elasticity of tailored springs. The origami metastructure can then locally control the contact of a device to the heat sink to displace heat or not by shape transition. As a result, the proposed switch regulates the device's temperature between designated temperatures, turning on and off automatically without the need for external sensory information and energy input. Our results demonstrate a significant enhancement in thermal modulation performance, with robust and energy-efficient operation under ambient conditions, paving the way for next-generation thermal management systems.

## Results

The ultra-high switching ratio originates from the bistable origami switch (BOS) from the two distinct stable states: the flat state (ON state) and the elevated state (OFF state). The two stable states display huge difference in thermal conductance (Fig. 1b). When the hosted device is heated up, the heat drives the origami metastructure to

overcome the energy barrier to shift from its elevated state to its flat state, and turn on the heat exchange with the heat sink (Fig. 1a). When the device cools down, the elastic force recovers the origami metastructure to the elevated state and turn off the heat exchange. By continuously repeating these steps, the temperature of a device is kept within the proper range passively.

The origami pattern of the BOS is illustrated in Fig. 1c, which is composed of five axisymmetric arms and a pentagon central panel. A design paradigm for the geometry is proposed, as illustrated in Fig. S1 (Supplementary Note 1). It is generated from three concentric polygons with different radius and the connection lines between their corresponding vertices. It is a special origami structure that features developability and chiral geometry, known as the Rotational Erection System<sup>44</sup>. Counting the degrees of freedom of the origami structure suggests that it is over constrained, leading to inherent bistability. When the arms stand up from the initial flat configuration, the pentagon panel is rotated and elevated evenly (Supplementary Video 1). The arms are under compression during the elevation process, which contributes to the energy barrier between the two stable states. The origami pattern is designed under four parameters:  $a$ ,  $c$ ,  $\alpha_1$ , and  $\alpha_2$ , as shown in Fig. 1c. The parameters  $a$  and  $c$  are derived from the overall dimensions of the device and the switch. The parameters  $\alpha_1$  and  $\alpha_2$  determine the height and the arm width of the structure, as illustrated in Fig. S2.

The polyimide sheet with a thickness of 0.2 mm was selected as the based material to fabricate the structure. We measured the Young's modulus of the polyimide sheet to be 4000 MPa, as shown in Fig. S4 (Supplementary Note 3). The origami structure is fabricated in three steps (Fig. 1d). First, we use a laser cutter to cut the polyimide sheet following the origami pattern, with all folding creases and cutting edges trimmed off. Second, we use pre-glued polyimide tape (0.06 mm) to coat the polyimide panels and reconnect the creases and edges. Finally, the polyimide tape is trimmed again only along the cutting edges. By this way, the rotational stiffness of the folding creases is extremely reduced (0.0285 N-mm/rad, Fig. S5). Results from the mechanical test of the origami structures show consistent bistable characteristics, including peak forces and location of the instability

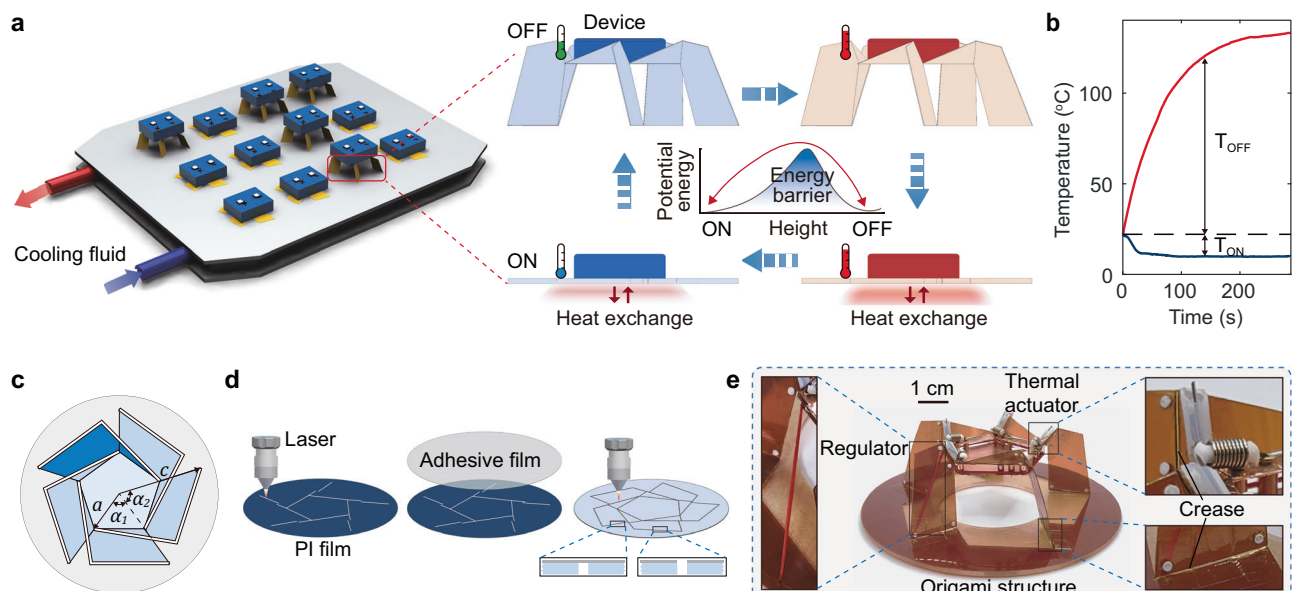


**Fig. 1 | Design and fabrication of the bistable origami switch (BOS).**

**a** Application and schematics of the BOS. Left: the BOS for pixelated thermal regulation of a battery pack. Right: a passive thermal regulation cycle. Heating the device over temperature threshold drives the BOS to overcome the energy barrier and transition from OFF to ON state, activating heat exchange with the heat sink,

while cooling reverses it via elastic force, turning off the heat exchange. **b** Real-time temperature profile at the ON and OFF states, respectively. **c** Origami crease pattern design. The thin black lines refer to folding creases, and the thick white lines are cutting edges. **d** Fabrication of the BOS using a laser cutter. **e** Photograph of a BOS at the OFF state with zoom-in views of the details.

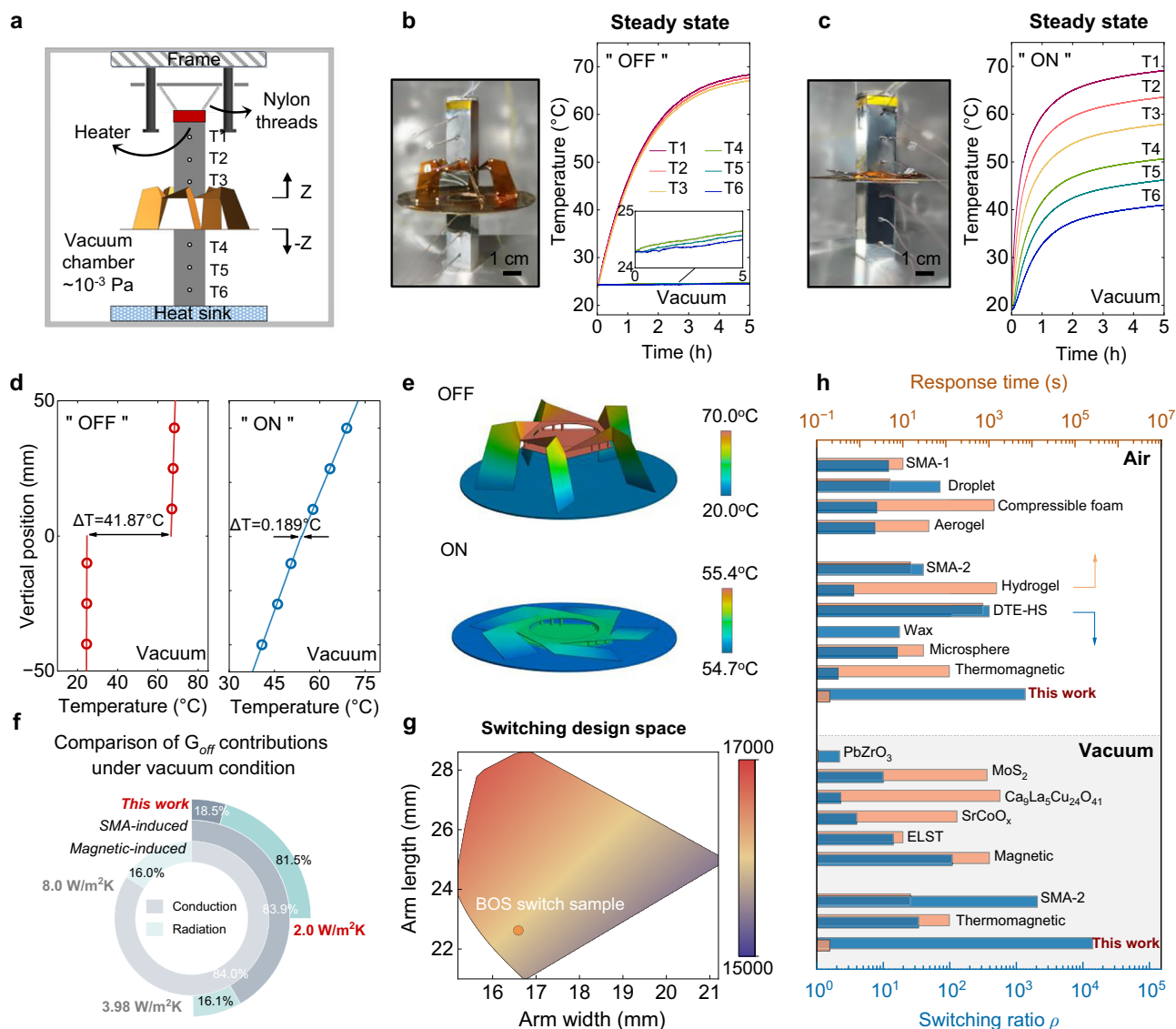


**Fig. 2 | Thermal switching ratio validation.** **a** Schematic of the high-vacuum steady-state thermal test platform. The setup consists of upper and lower stainless steel reference bars; each embedded with three high-precision thermocouples. The lower bar interfaces with a heat sink, while the upper bar incorporates a Joule heater and is suspended from the frame by thermally insulating nylon threads attached to its top surface. The BOS is sandwiched between the two reference bars. **b, c** Photographs of the test setup in ON/OFF states, and the temperature-time profiles recorded by the six thermocouples. **d** Steady-state temperature distributions along the bars for the ON/OFF states. Interfacial temperature discontinuities

( $\Delta T_{on/off}$ ) are determined via linear extrapolation of bar temperatures. **e** Temperature distributions of the BOS by finite element simulations. **f** Comparative analysis of the off-state conductance ( $G_{off}$ ) in vacuum between this work and other representative contact-based thermal switches, where the contributions from conduction/radiation pathways are highlighted. **g** Theoretical switching design space, showing the dependence of the switching ratio on arm width and height. **h** Performance benchmarking against existing active and passive thermal switches<sup>11,14,15,46,49-60</sup>, comparing switching ratios ( $\rho$ ) and response times under vacuum/ambient conditions (Table S2).

point, across different fabrication batches (Fig. S6, Supplementary Note 3), attesting to the repeatability of the manufacturing process and the robustness of the design.

After equipped with the thermal actuators and the regulator, we obtain the functional BOS (Fig. 1e). Figure S3 (Supplementary Note 2) presents the specific components employed and the detailed compositional procedure. Each arm is embedded with a custom thermal actuator to drive the switching in response to excessive heat over the temperature threshold.

To experimentally measure the thermal conductance of the two states of the BOS, we employed the widely recognized reference bar method<sup>45</sup>. A high-vacuum steady-state thermal conduction platform was constructed in compliance with the ASTM-5470 standard, and a schematic of the experimental setup is illustrated in Fig. 2a. The BOS

was positioned between two stainless steel reference bars—serving as heat source and sink—each embedded with three equidistant high-precision thermocouples along their lengths to ensure a one-dimensional heat flow. Photographs of the experimental setup along with a corresponding close-up image are illustrated in Fig. S9 (Supplementary Note 4). Figure 2b, c show photographic images of the test apparatus in its ON and OFF states, as well as the corresponding temperature-time profiles recorded by the thermocouples. Figure 2d presents the steady-state temperature distributions along the reference bars in both switching states.

The thermal conductance values ( $G_{on/off}$ ) were calculated using Fourier's law,  $G_{on/off} = q/\Delta T_{on/off}$ , where the interfacial temperature drop  $\Delta T_{on/off}$  was determined by linear extrapolation of bar temperature profiles, and the heat flux  $q$  was derived from the temperature

gradient in the lower bar. The thermal switching ratio ( $\rho = G_{on}/G_{off}$ ) serves as a key performance metric. In the OFF state, a substantial temperature discontinuity of  $\Delta T = 41.87^\circ\text{C}$  was observed across the BOS, corresponding to an ultralow thermal conductance of  $G_{off} = 2.0\text{ W/m}^2\cdot\text{K}$ . Upon switching to the ON state, the origami-enabled mechanical contact significantly reduced the interfacial resistance, resulting in  $\Delta T = 0.189^\circ\text{C}$  and an exceptionally high conductance of  $G_{on} = 27,968\text{ W/m}^2\cdot\text{K}$ . These values yield an unprecedented switching ratio of  $\rho = 13,984$  under vacuum conditions—the highest reported to date for a passive thermal switch. Finite element simulations (Fig. 2e) further corroborate the experimental findings, showing distinct and consistent temperature distributions for the ON and OFF states within the reference bar assembly. To assess real-world applicability, the same measurements were conducted under atmospheric conditions. Despite the presence of parasitic heat transfer through air conduction and convection, which leads to the OFF state conductance to  $G_{on} = 51,685\text{ W/m}^2\cdot\text{K}$  and  $G_{off} = 38\text{ W/m}^2\cdot\text{K}$  (Fig. S10, Supplementary Note 5), respectively, the BOS achieved a switching ratio of 1360—still several orders of magnitude greater than existing passive thermal switching solutions.

To elucidate the physical origins of the exceptionally high switching ratio of the BOS, we developed a theoretical thermal conductance model based on the reference bar experimental setup (Supplementary Note 6). Under vacuum conditions, heat transfer between the upper and lower bars occurs through two primary pathways: radiative heat exchange and solid conduction via the BOS (Fig. S11, Table S1). The model predicted an OFF state thermal conductance of  $G_{off} = 1.75\text{ W/m}^2\cdot\text{K}$  and a switching ratio  $\rho = 15,982$ , closely aligning with the experimental value of 13,984. The remaining discrepancy is primarily attributed to uncertainties in estimating surface emissivity. Decomposition of  $G_{off}$  reveals that solid conduction contributes only  $0.37\text{ W/m}^2\cdot\text{K}$ —approximately 18.5% of the total—significantly lower than that of state-of-the-art contact-based thermal switches. For comparison, a typical SMA-spring thermal regulator exhibits  $G_{off} = 3.98\text{ W/m}^2\cdot\text{K}$ , with solid conduction accounting for 83.9% of the total<sup>15</sup>; a representative magnetic thermal transistor shows  $G_{off} = 8.0\text{ W/m}^2\cdot\text{K}$ , with 84.0% attributed to solid conduction<sup>46</sup> (Fig. 2f, Table S2). We further evaluated multiple candidate base materials for the BOS with different thermal conductivities (e.g., PC, PVC, PET, PS, and silica aerogel, summarized in Fig. S11). Each of these materials shows a high switching ratio, ranging from  $1.6 \times 10^4$  to  $2.0 \times 10^4$  in vacuum, which confirms the broad material compatibility of the BOS design.

Unlike prior designs with immediate connection between the thermal reservoirs via thermally conductive solid elements (e.g., SMA or polymer pins), the BOS employs a bistable origami metastructure in which the SMA hinges are isolated at the folding creases and do not bridge the hot and cold surfaces. Thus, the thermal path in the off-state is dominated by the thin polyimide film (with ultralow thermal conductivity,  $k = 0.2\text{ W/m}\cdot\text{K}$ ) and a large spatial gap (16 mm), effectively suppressing both heat conduction and convection. Moreover, the BOS design features geometrically tunable parameters—such as arm width, length, and height—that allow for programming of the switching ratio across a broad range ( $\rho = 15,425$  to  $16,771$ , Figs. 2g, S12). Combined with its relatively fast response time, the BOS not only outperforms existing passive thermal switches but also exceeds the performance of many active ones (Fig. 2h and Table S2), demonstrating its transformative potential for next-generation thermal management applications.

To switch between the two stable states, an energy barrier must be overcome by the thermal actuators. We developed an analytical model to study the energy evolution of the origami structure during deformation (Supplementary Notes 7 and 8). The model accounts for the folding energy localized at the hinges and the bending energy along the arms. The analysis began by examining the kinematics of the hinges and the upper plate. The results confirm that the folding at the

bottom hinges, along with the resulting displacement and rotation of the upper plate, undergoes rigid-body motion, as shown in Fig. S13. In contrast, the folding at the upper hinges is affected by the bending of the arms. To investigate the bending energy, the arm of the origami structure is simplified as a beam element and analyzed using Timoshenko beam theory. The beam model, employed to simulate the arm under shear or compression, yields results that closely match the finite element simulations (Figs. S14–S16). The stress distribution results from the finite element simulations are presented in Fig. S17, revealing significant localized stress intensity in the arm and crease regions. The stress concentrations mainly occur at the bottom creases, reaching a maximum Von Mises stress of 129 MPa. Furthermore, five origami samples with different geometrical parameters were fabricated to validate the analytical model experimentally (Fig. S18).

Through quantitative analysis by the analytical model, we investigate the bistable energy landscape and the design scope of the origami structure (Supplementary Note 9). The geometric parameter  $\alpha_2$ , which governs the folding direction of the arms, directly determines whether the structure exhibits bistability. As  $\alpha_2$  increases, the energy barrier of bistability emerges, increases, then decreases, and finally disappears (Fig. S19). Along with the geometric parameter  $\alpha_1$ , the energy barrier varies from 0 mJ to 1 mJ. To achieve a higher barrier, the radius of the middle pentagon (Fig. S1) can be increased, raising the energy barrier to 4 mJ. Fig. S20 further illustrates the bistable origami structure within the ( $\alpha_1$  and  $\alpha_2$ ) parameter space: arm width is bounded between 15–21.5 mm, while standing height ranges from 16 to 26.3 mm.

Meanwhile, the analytical model verifies that the origami structure exhibits a deformation pattern with approximately one degree of freedom. Actuating any hinge can drive the entire structure for state toggling. We select the folding creases between the arms and the pentagon panel to install the thermal actuators (Fig. 3a) so that they are close to the hosted device (i.e., heat source) for efficient heating. The actuation force by the thermal actuators varies as the temperature and the elevated height ( $\delta$ ) changes, demonstrating a vertical driving force of 1.2 N at  $80^\circ\text{C}$  and  $-0.5\text{ N}$  at  $25^\circ\text{C}$  (Fig. 3b). The experimental setup for measuring the actuation force is provided in Fig. S8 (Supplementary Note 3). In this procedure, the BOS is clamped in a fixed position. The actuators are then heated by a heater, and the vertical load is measured concurrently.

The thermal actuator composes of a nickel titanium (NiTi) SMA wire and an elastic torsional spring (Fig. 3c), which provides bidirectional driving torque at low and high temperature thresholds. The driving torque is from the difference of the torques of the SMA wire and the torsional spring. The SMA wire has an initial Z-shape at low temperature and twists  $90^\circ$  towards a U-shape upon heating above its phase transition temperature. The maximum actuation torque of the SMA wire is measured to be 5 N-mm at  $70^\circ\text{C}$  (Fig. 3d). When the temperature of SMA wire decreases below  $25^\circ\text{C}$ , the active driving torque vanishes, and the SMA wire is left with a nearly constant passive resistance of 0.86 N-mm. On the other hand, the torsional spring has an elastic torque of 1.9 N-mm/rad with a rest angle at the elevated OFF state. Its elastic torque is capable of untwisting the SMA wire back to its Z-shape. However, as  $\gamma$  decreases towards the elevated state, the elastic torque of the torsional spring decreases linearly, and reaches an equilibrium with the resistance of the SMA wire at  $147^\circ$  (Fig. 3d).

Furthermore, taking into account the bistable energy barrier of the origami structure, it is clear that the driving force of the thermal actuator at low temperature is not enough to push the BOS from ON state to OFF state. To address this problem, an elastic regulator (i.e. a TPU cord) is adopted to adjust the energy barrier of the origami metastructure. The regulator is connected between the ends of the upper plate and the base (Fig. 3a). When the BOS switches from the elevated to the flat state, the upper plate rotates relative to the base, stretching the regulator and increasing its tensile strain from 0 to 0.19

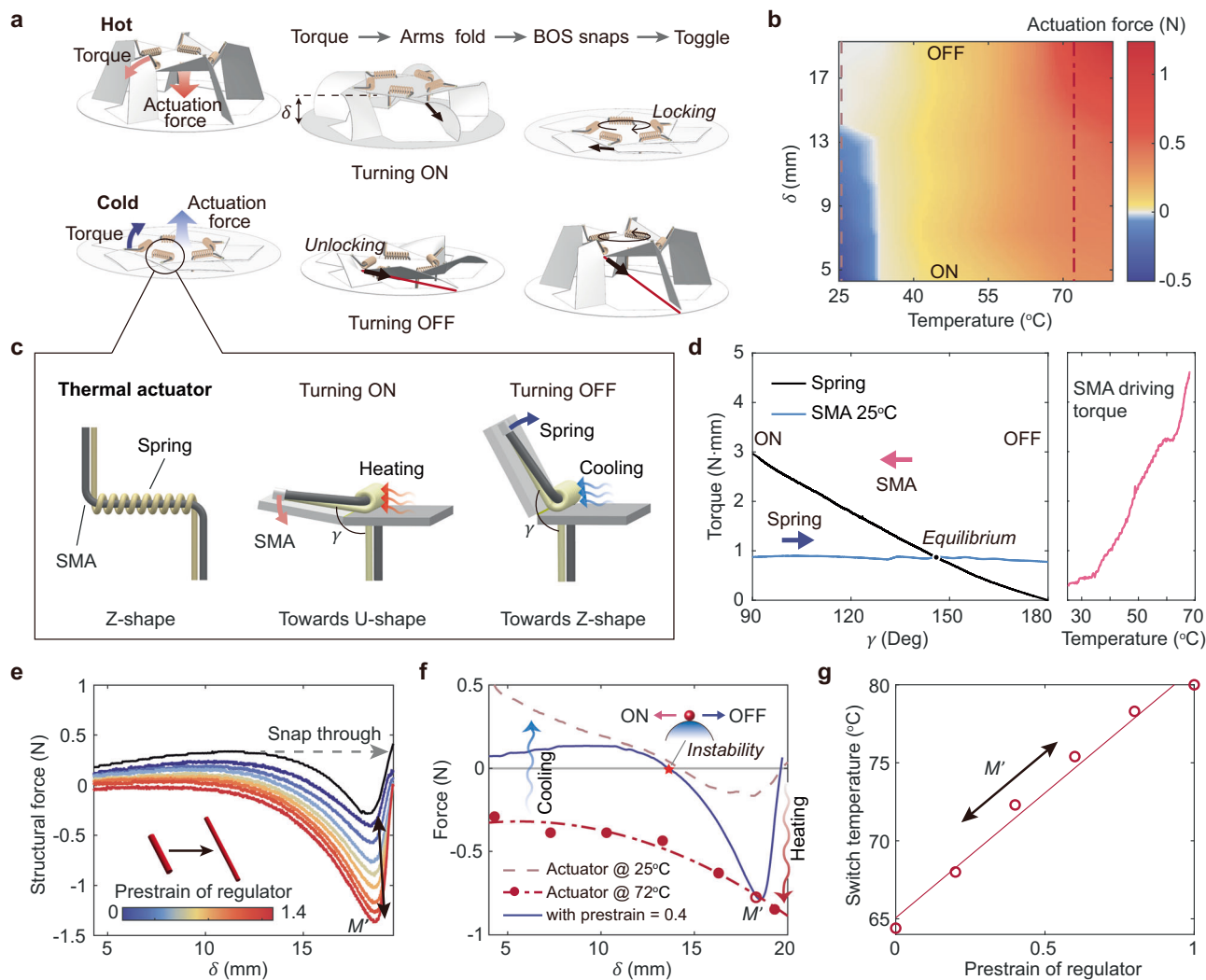


**Fig. 3 | Working principle and tunability of the BOS.** **a** Switching mechanism of the BOS, driven by the custom thermal actuators. **b** Total actuation force of thermal actuators on BOS as a function of temperature and height. **c** Design of the thermal actuator. The SMA wire generates actuation torque that overrides the elastic torsional spring at high temperature, while their roles are reversed at low temperature (Supplementary Video 2). **d** Experimentally measured torque of the torsional spring and the SMA wire versus rotation angle  $\gamma$ . **e** Structural force of the origami metastructure with regulator under various prestrains versus elevation height  $\delta$ .

The points  $M'$  indicate the negative peak forces during the snap-down process (i.e., turning ON). **f** Balance between the actuation force of the thermal actuators and the structural force of the origami metastructure (with regulator). The allowable temperature range is set as 25–72 °C. The curve representing structural force must be clamped between the two actuations curves at high and low temperatures to enable successful state switching. **g** Tunable range of the high switching temperature by adjusting the prestrain of the regulator.

(Fig. S21, Supplementary Note 10). Thus, at low temperature and the ON state, the regulator adds extra force to pull the BOS up, and equivalently, reduces the critical force required to overcome the energy barrier to elevate (i.e., turning OFF). As shown in Fig. 3e, by increasing the prestrain of the regulator at the elevated state of the BOS, the critical structural force of the BOS is effectively reduced for switching OFF (Supplementary Video 1). The experimental setup for measuring the structural force and the preloading strain of the regulator is depicted in Fig. S7 (Supplementary Note 3). The influence of the regulator on the energy barriers of the BOS is illustrated in Figs. S21 and S22. The results demonstrate that the regulator not only reduces the first energy barrier but also strengthens the second one, thereby enabling an extension of the bistable energy landscape by up to 40%.

To realize full cycles of the BOS, the driving force of the thermal actuators and the resistance of the origami metastructure must be carefully calibrated (Fig. 3f). We must ensure that the actuation forces at both the high and low switching temperatures are larger in magnitude than the critical structural forces to overcome bistable energy

barrier. In other words, the structural force curve must be clamped by the two actuation force curves, as shown in Fig. 3f. When the actuation force exceeds the negative peak force ( $M'$ ), the thermal actuators push the BOS to snap down and turn ON. Conversely, when the temperature becomes lower than 25 °C, the reverse actuation force exceeds the positive peak force, and the BOS is elevated and turned OFF.

Tuning the prestrain of the regulator changes the structural force profile of the BOS (Fig. 3e), and thus adjusts the switching temperatures. To elaborate, as the prestrain of the regulator increases, the critical peak force linearly increases (Fig. S23), and the required actuation force increases accordingly, leading to higher switching temperature (Fig. 3g). In addition to the prestrain of the regulator, customizable switching temperatures can also be achieved by changing the phase transition temperature of the SMA. For example, if we change the phase transition temperature of the SMA from 60 °C to 47 °C, the high switching temperature decreases from 73 °C to 63 °C (Fig. S26 and Supplementary Video 2).

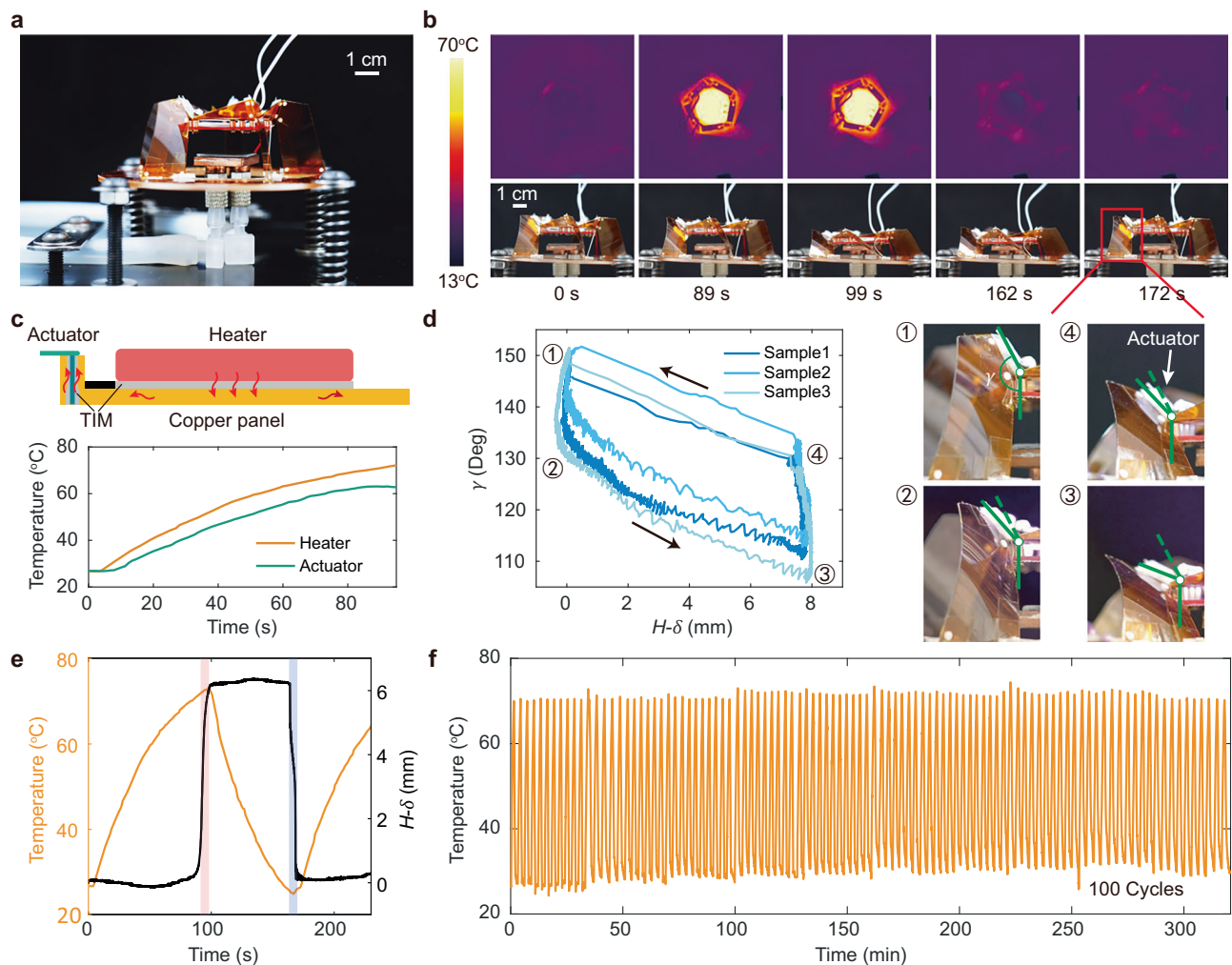


**Fig. 4 | Demonstration of the functionality and switching of BOS.** **a** Photograph of the customized experimental setup. The heat source is hosted on the upper plate of the BOS. A water-cooled plate is installed underneath the BOS as the heat sink. **b** Video frames and IR images of the BOS during one cycle of temperature regulation. **c** Schematic of the heat flow on the upper plate, and the temperature changes of the heater and the actuator. **d** Hinge actuation process for switching

recorded as vertical displacement ( $H-\delta$ ) vs. dihedral angle ( $\gamma$ ), where  $H$  is the initial height of the device at the elevated OFF state. **e** Real-time temperature profile and vertical displacement ( $H-\delta$ ) of the hosted device. **f** Repeatability test of the BOS up to 100 times. The temperature of the Joule heater is well controlled within 28.2–71.7 °C.

In our experimental demonstration (Fig. 4, Supplementary Video 2), the low and high switching temperatures are set as 25 °C (ON → OFF) and 72 °C (OFF → ON), respectively (Figs. 3e, S24, Supplementary Note 11). The setup is in ambient air and composed of the BOS, a heater, and a heat sink (Fig. 4a). The heat sink is a 2 cm × 2 cm water-cooled copper plate with a constant temperature controlled at 4 °C. An 1 mm-thick, aluminum nitride-filled thermal conductive silicone sheet is applied on the copper plate to enhance thermal contact with the hosted device at ON state. To test the cyclic performance of the BOS, a standard ceramic Joule heater is first used, under 5 V-applied voltage. The BOS automatically toggles ON and OFF according to the switching temperatures (Fig. 4b). Figure 4c illustrates the heat transfer from the heater to the thermal actuator via the copper panel. This design results in a temperature difference of 7 °C between the heater and the actuator when the heater is heated to 70 °C.

The relationship between the driving angle of the thermal actuator and the vertical displacement of the upper plate is plotted in Fig. 4d. During operation, the actuator undergoes a total driving angle of approximately 40 degrees at each stroke. It first folds by 20 degrees to build up actuation force, then drives the BOS upward or downward through the subsequent 20 degrees. This behavior confirms that the

BOS effectively locks into position at both the ON and OFF states, without getting stuck in some intermediate states. Figure 4e displays the real-time temperature and displacement curves of the BOS. The data show that the BOS remains stable in either the ON or OFF state until the temperature reaches the switching threshold. The subsequent state transition exhibits a response time of ~10 s and a vertical speed of 0.66 mm/s (Fig. S25). The temperature regulation function is uncompromised after 100 cycles of continuous test, demonstrating outstanding reliability of the BOS (Fig. 4f). During the repeated cycles, the high and low switching temperatures remain very stable, measured as  $71.7 \pm 1.7$  °C and  $28.2 \pm 3.4$  °C, respectively. The repeatability of the fabrication process is highlighted by the batch-to-batch consistency observed in the switching temperature and operational characteristics, as shown in Fig. S27.

The switching speed of the BOS is influenced by a number of factors, including travel distance between the ON and OFF states, the number of thermal actuators, heat sink temperature, the heating rate, and the bearing mass on the upper plate. It was found that the travel distance plays a primary role affecting the switching speed of the BOS. Using a high-speed camera (X190, Reveal, China) to capture the pure structural snap-through transition of the origami structure (Fig. 5a), we

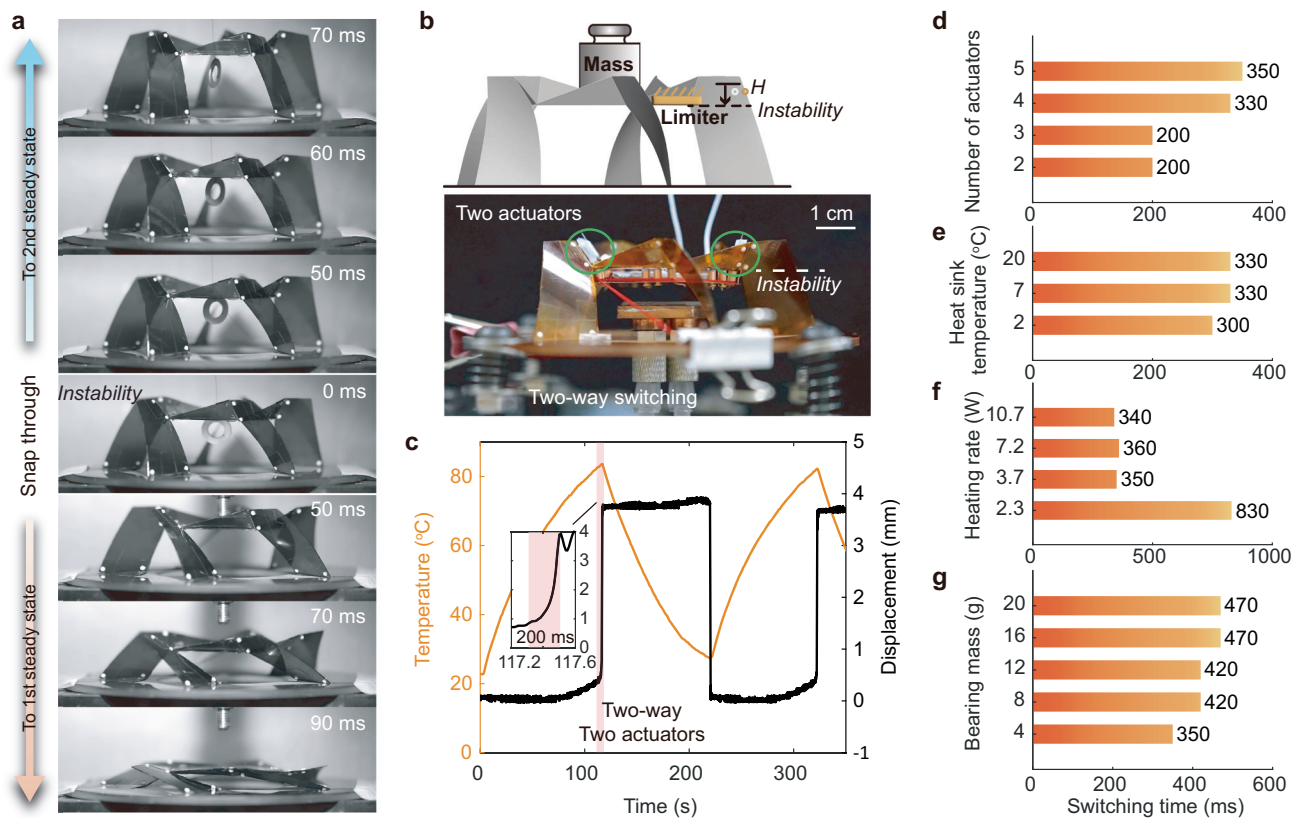


**Fig. 5 | Factors affecting the switching speed of the BOS.** **a** Video frames of the snap-through transition of the origami structure only, captured by high-speed camera. **b** Setup for the switching speed test. A weight is added on the upper plate to investigate the influence of bearing weight. An additional limiter is used to

investigate the influence of bistable position. **c** Real-time temperature profile and vertical displacement of the two-way switching. **d–g** Factors that affect the switching speed, including: number of actuators, heat sink temperature, heating rate, and bearing mass.

observe that traveling from the instability point to any stable state requires less than 90 ms. To exploit this property, we equipped the BOS with a limiter that constrains the upper plate to become 3 mm closer to its instability point than before (Fig. 5b). With the limiter and two thermal actuators, the BOS achieves two-way operation with a switching time of 200 ms (Fig. 5c), with switching temperature at 83.6 °C.

The influence of the number of thermal actuators on the switching speed is presented in Fig. 5d. The results indicate that a greater number of actuators leads to an increase in the switching time, owing to the increased resistance force of the system. A slow-motion video of the BOS equipped with five actuators is provided in Supplementary Video 3. For the BOS equipped with only one thermal actuator, the generated actuation force was insufficient to drive the bistable switching. Influences of the heat sink temperature, the heating rate, and the bearing mass on the upper plate are shown in Fig. 5e–g. While changing the heat sink temperature and the heating rate exhibit no significant trend, we find that larger bearing mass on the upper plate leads to slower transition, likely due to larger inertia.

To investigate the influence of bearing mass, we conducted a series of experiments by adding calibrated weights onto the upper plate of the BOS. As the load increased, the transition from the ON to OFF state became more challenging due to the increased weight and inertia. To address this, we can raise the pre-strain in the regulator, thereby boosting the restoring force at the ON state to support heavier loads. As a result, even under a total mass of 20 g, the BOS maintained a functional snap-through transition, with a switching time of 470 ms, as presented in Fig. 5g and the Supplementary Video 4.

To showcase the versatility of the BOS in real world applications, we experiment the BOS for temperature regulation of some commonly used electric devices, including battery, power amplifier, Bluetooth chip, LED, and DC-DC converter (Fig. 6a, Supplementary Video 5). The BOS displays its passive, automatic switching function to these devices, and successfully regulates the temperature of the devices in a certain range (Fig. 6b–e). The designated temperature range of the power amplifier, LED, and DC-DC converter are tuned to be around 24–77 °C. Since the heating effect of the Bluetooth chip is much higher, the maximum switching temperature is increased to 114.5 °C. In contrast, the lithium-ion battery has stringent temperature requirements to avoid permanent damage. As a result, the thermal actuator is built with low temperature SMA of 47 °C, such that the corresponding BOS maintains a steady temperature regulation around 27–67 °C (Fig. 6f). The BOS design also shows quite consistent thermal switching performance with different numbers of arms, as shown in Fig. 6g–h and Supplementary Video 6. The switching time of the four-arm and six-arm BOS are 7.2 s and 90 ms, respectively, demonstrating a notable decrease as the number of arms increases in the range that we have tested. During the snap-through transition, the top plate remained flat relative to the ground given different number of arms.

## Discussion

In this work, we leverage bistable origami metastructures to create a thermal switch that demonstrates unprecedented switching ratio (1360 in air, 13,984 in vacuum), passive operation (response time ~200 ms), and exceptional cyclic reliability. The novelty of this work is two-fold: (1) This work reports a mechanical thermal switch using bistable origami structure that produces record-high switching ratio

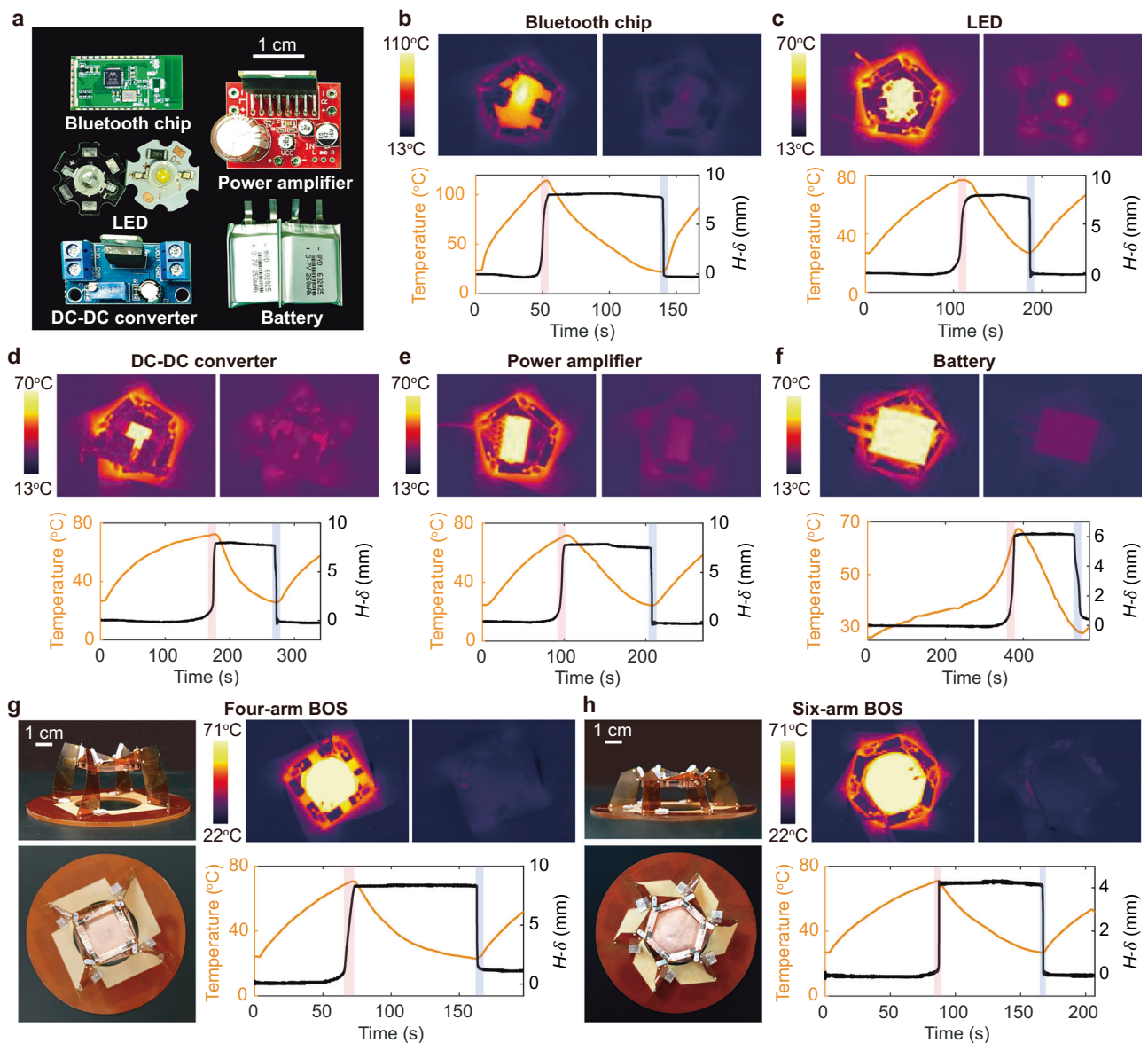


**Fig. 6 | Effectiveness of the BOS for temperature regulation.** **a–f** Demonstration of the BOS hosting various devices, including battery, power amplifier chip, Bluetooth chip, LED, and DC-DC converter chip. **g, h** Functionality of the BOS with four-arm and six-arm configurations.

among all types of thermal switches (Fig. 2, Supplementary Table S2); The ultra-high switching ratio arises from mechanically driven transitions between two thermally distinct stable states, enabled by instability-induced deformation. (2) The repeatable passive thermal regulation cycles highlight that the complete BOS is no longer mechanically bistable in the conventional sense; rather, its bistability emerges at the system level under thermal loading (Fig. 3). The switching mechanism is entirely passive, facilitated by a novel temperature-sensitive actuator system comprising SMA and elastic springs. As a result, the proposed bistable origami switch (BOS) can autonomously regulate the local temperature of power electronics across repeated cycles, offering precise control over operational temperature ranges without external power input. Compared to conventional thermal switches that suffer from low switching ratios and lack of bistable behavior, the BOS combines high contrast in thermal conductance with threshold-defined operation, ensuring robust performance under environmental noise and fluctuations. Furthermore, as the bistable behavior mainly comes from geometry, our solution is inherently scale-independent, which can be potentially scaled up and down from meters to micrometers<sup>36,47</sup>.

Considering the fabrication and assembly of thermal actuators, in the micro-scale, the torsion springs may be replaced by the inherent elasticity of the origami hinges, and the SMA wires can be replaced by other printable or depositable stimuli-responsive materials<sup>47,48</sup>. Future work is still needed to unleash the high suitability of the BOS for integration in advanced chip architectures. These findings demonstrate how the integration of smart structural mechanics and responsive materials can enable physically intelligent thermal management devices, paving the way for scalable, pixelated, and self-powered thermal control systems.

As the power density of advanced electronics continues to rise—driven by high demands of robotics, AI computing clusters, the Internet of Things, and electric vehicles—thermal management has emerged as a critical bottleneck for maintaining reliable performance. This underscores the urgent need for dynamic and reversible thermal switches capable of localized, on-demand heat control. The BOS developed in this work offers a compelling solution. Moreover, its bi-stability not only enables passive switching between distinct thermal states but also mirrors binary logic (0 and 1), making it particularly suited for thermal logic circuits, where non-volatile state

retention is a foundational requirement. The scalable, passive, self-regulating operation of the BOS holds strong potential for enabling self-sustained and self-adaptive thermal bits, laying the groundwork for future thermal computing architectures. By integrating principles from materials science, heat transfer, and mechanical design, these origami-enabled thermal switches represent a frontier in physically intelligent systems for advanced thermal management and computing.

## Methods

### Sample fabrication

A 0.2-mm-thick polyimide film (Guangzhou Shibe Dragon Electronics Co., Ltd., China) is selected as the base material. The film is laser-cut along the origami pattern (Fig. 1d) using a 16 W laser cutter. The design parameters of the origami pattern are set as  $a = 20$  mm,  $b = 25$  mm,  $c = 40$  mm,  $\alpha_1 = 59.2^\circ$ , and  $\alpha_2 = 55^\circ$ . Cut pieces are bonded using polyimide tape (3 M™ 7418 F Heat-Resistant Polyimide Process Tape). Fifteen 1-mm-diameter holes are drilled into the inner pentagon panel (three holes at each edge).

The thermal actuator (Fig. 3c) comprises a U-shape SMA wire (Beijing GEE SMA Technology Co., Ltd., China) and a stainless-steel torsional spring (Wenzhou Heli Spring Manufacturing Co., Ltd., China). The U-shape SMA wire has a length of 7.5 mm, width of 5 mm, and wire diameter of 0.5 mm. It is twisted  $180^\circ$  about its major axis and installed concentrically within the torsional spring. The torsional spring has a wire diameter of 0.4 mm, outer diameter of 3 mm, 9 coils, and an initial angle of  $180^\circ$ .

To mount the thermal actuator and facilitate heat transfer, a copper base is fabricated using a 0.1-mm-thick copper plate (Xinghua Fangling Metal Products Co., Ltd., China) and copper sleeves (Taizhou Xuehua Stainless Steel Products Co., Ltd., China). The copper plate is cut to size matching the dimensions and arrangement of the inner pentagon pane. Copper sleeves (height: 3 mm, inner diameter: 1 mm, outer diameter: 2.2 mm) are welded over these holes. The sleeve bores are then filled with silicone grease (Shin-Etsu Chemical 7921), and a 0.8-mm-diameter TPU elastic cord (MIYUKI H3198E, length: 50 mm) is fastened to a corner sleeve. This integrated assembly of copper plate, sleeves, and TPU cord constitutes the regulator.

Finally, the regulator's sleeves and TPU cord are secured to the polyimide film. The thermal actuators are installed by inserting their wire ends into the copper sleeves, while the opposite ends engage mounting tubes. These mounting tubes are sections of Teflon tubing (inner diameter: 1.8 mm, outer diameter: 2.6 mm) cut to length of 5 mm. The Teflon tubes are permanently affixed to the origami arms via riveted connections.

### Thermal switching ratio measurements

The thermal characterization of the bistable origami switch (BOS) is conducted using a custom-built testing platform (Fig. 2a and Fig. S9), designed in accordance with ASTM-5470 standards. Measurements are conducted inside a sealed aluminum vacuum chamber under high-vacuum conditions of  $-10^{-3}$  Pa. The setup consists of two vertically aligned stainless steel reference bars ( $20 \times 20 \times 50$  mm) with precision-ground surfaces ( $R_a \leq 0.025$ ) to minimize radiation losses. The lower bar is fixed to the chamber base, while both bars are instrumented with three T-type thermocouples ( $\pm 10$  mK accuracy,  $254 \mu\text{m}$  diameter) spaced 15 mm apart to record temperature gradient. Temperature data is recorded by two YET-640X four-channel thermometers. The BOS sample is tightly aligned between the reference bars using press-fit assembly, ensuring flush contact with the bar ends for efficient thermal coupling. An alumina-based ceramic heater is mounted on the top surface of the upper reference bar to provide a controlled heat input. For OFF-state measurements, the upper bar is suspended using nylon threads to eliminate contact (Fig. S9A). For ON-state measurements, it is lowered into direct contact with the lower bar (Fig. S9B). To

enhance interfacial thermal conductance, a thin ( $\sim 100 \mu\text{m}$ ) layer of Apiezon H high-vacuum grease is applied at the contact interface.

The thermal conductance of the BOS in ambient air is measured using the same experimental platform and protocol as in vacuum conditions, with two key procedural modifications. First, the vacuum chamber is vented to atmospheric pressure (1 atm) while maintaining a hermetically sealed environment. Second, the thermal interface material (TIM) is changed. For vacuum measurements, a low-vapor-pressure TIM (Apiezon H) with a relatively low thermal conductivity of  $0.216 \text{ W/m}\cdot\text{K}$  is used to avoid outgassing. In contrast, air-based measurements allow the use of high-performance TIMs, such as Shin-Etsu X-23-7921-5, a commercially available thermal grease with a significantly higher thermal conductivity ( $>6 \text{ W/m}\cdot\text{K}$ ), thereby minimizing interfacial thermal resistance.

It is noteworthy that thermal radiation losses along the reference bars are proportional to the fourth power of local temperature, resulting in slight non-uniformities in vertical heat flux. Due to its closer proximity in temperature to the ambient environment, the lower reference bar experiences reduced radiative loss and more closely satisfies the assumption of a linear temperature distribution. Therefore, the temperature gradient used to compute thermal conductance via Fourier's law  $G = Q/\Delta T$  is obtained from a linear fit of the temperature distribution along the lower bar. Detailed temperature distributions, extracted thermal conductance values, and corresponding switching ratios under vacuum conditions are presented and discussed in the main text.

### Structural force measurements

To measure axial force while accommodating twist coupling in the BOS, we fabricated a low-friction rotational coupling between the BOS and testing machine clamp (Fig. S6). The coupling consists of a pentagonal copper plate mounted at the terminus of a slender bolt, constrained by locking nuts and washers. During testing, the BOS is initialized in its flat state, and then being vertically deployed at  $10 \text{ mm/min}$  via the clamp. Throughout deployment, axial displacement and force are recorded.

The same experimental setup is used to measure structural forces on the BOS with regulator. One end of the regulator is secured to a corner of the BOS pentagon panel, while the opposite end passes through a base plate mounting hole. A steel caliper is fixed to the base plate serves as the measurement reference. During testing, predetermined prestrain is applied by stretching the regulator to align with the caliper's target scale. Final positioning of the regulator is maintained using two mechanical clamps.

### Actuation force measurements

To measure thermal actuation forces across temperatures, the BOS is equipped with a heater, five thermal actuators, and a thermocouple. The testing machine operates in position-holding mode, lowering the BOS to a predetermined height  $\delta$  and taring the force sensor. A constant 5 V voltage is applied to the heater while force-time and temperature-time profiles are synchronously recorded. Force-temperature curves are generated by cross-referencing the time-synchronized datasets. This procedure is repeated for multiple displacement setpoints  $\delta$  to characterize the temperature-dependent force response.

To obtain the actuation force-displacement curve of the BOS at  $25^\circ\text{C}$ , we first measure the force-displacement curve of the BOS with thermal actuators at  $25^\circ\text{C}$ , then subtract the baseline structural response without thermal actuators.

### Data availability

The data that support the findings of this study are provided in the main text and the Supplementary Information. Source data are provided with this paper.

## References

1. Li, N. et al. Colloquium: phononics: manipulating heat flow with electronic analogs and beyond. *Rev. Mod. Phys.* **84**, 1045–1066 (2012).
2. MacCabe, G. S. et al. Nano-acoustic resonator with ultralong phonon lifetime. *Science* **370**, 840–843 (2020).
3. Chen, G. Non-Fourier phonon heat conduction at the microscale and nanoscale. *Nat. Rev. Phys.* **3**, 555–569 (2021).
4. Qian, X., Zhou, J. W. & Chen, G. Phonon-engineered extreme thermal conductivity materials. *Nat. Mater.* **20**, 1188–1202 (2021).
5. Chen, Q. et al. Adaptive metaskins for active and passive thermal camouflage. *Adv. Mater.* **38**, e06934 (2025).
6. Yang, L. et al. Suppressed thermal transport in silicon nanoribbons by inhomogeneous strain. *Nature* **629**, 1021–1026 (2024).
7. Shin, J. et al. Light-triggered thermal conductivity switching in azobenzene polymers. *Proc. Natl. Acad. Sci. USA* **116**, 5973–5978 (2019).
8. Lee, S. et al. Anomalously low electronic thermal conductivity in metallic vanadium dioxide. *Science* **355**, 371–374 (2017).
9. Lu, Q. et al. Bi-directional tuning of thermal transport in SrCoOx with electrochemically induced phase transitions. *Nat. Mater.* **19**, 655–662 (2020).
10. Zhu, G. et al. Tuning thermal conductivity in molybdenum disulfide by electrochemical intercalation. *Nat. Commun.* **7**, 13211 (2016).
11. Liu, C. H. et al. Low voltage-driven high-performance thermal switching in antiferroelectric PbZrO thin films. *Science* **382**, 1265–1269 (2023).
12. Li, M. et al. Electrically gated molecular thermal switch. *Science* **382**, 585–589 (2023).
13. Novak, K. S., Phillips, C. J., Sunada, E. T. & Kinsella, G. M. Mars exploration rover surface mission flight thermal performance. *SAE Trans.* **114**, 118–129 (2005).
14. Guo, L., Zhang, X. S., Huang, Y., Hu, R. C. & Liu, C. L. Thermal characterization of a new differential thermal expansion heat switch for space optical remote sensor. *Appl. Therm. Eng.* **113**, 1242–1249 (2017).
15. Hao, M. L., Li, J., Park, S., Moura, S. & Dames, C. Efficient thermal management of Li-ion batteries with a passive interfacial thermal regulator based on a shape memory alloy. *Nat. Energy* **3**, 899–906 (2018).
16. Yasuda, H. et al. Origami-based impact mitigation via rarefaction solitary wave creation. *Sci. Adv.* **5**, eaau2835 (2019).
17. Liu, Z. et al. Origami-enhanced mechanical properties for worm-like robot. *Soft Robot* **12**, 34–44 (2024).
18. Ho, D. T., Kim, S. Y. & Schwingschlögl, U. Graphene origami structures with superflexibility and highly tunable auxeticity. *Phys. Rev. B* **102**, 174106 (2020).
19. Schenk, M. & Guest, S. D. Geometry of Miura-folded metamaterials. *Proc. Natl. Acad. Sci. USA* **110**, 3276–3281 (2013).
20. Pratapa, P. P., Liu, K. & Paulino, G. H. Geometric mechanics of origami patterns exhibiting Poisson’s ratio switch by breaking mountain and valley assignment. *Phys. Rev. Lett.* **122**, 155501 (2019).
21. Silverberg, J. L. et al. Using origami design principles to fold reprogrammable mechanical metamaterials. *Science* **345**, 647–650 (2014).
22. Guo, X. et al. Designing mechanical metamaterials with Kirigami-inspired, hierarchical constructions for giant positive and negative thermal expansion. *Adv. Mater.* **33**, 2004919 (2021).
23. Li, Y. et al. Adaptive hierarchical origami-based metastructures. *Nat. Commun.* **15**, 6247 (2024).
24. Wang, C. et al. Reconfigurable origami-inspired multistable metamorphous structures. *Sci. Adv.* **10**, eadk8662 (2024).
25. Dudte, L. H., Vouga, E., Tachi, T. & Mahadevan, L. Programming curvature using origami tessellations. *Nat. Mater.* **15**, 583–588 (2016).
26. Dieleman, P., Vasmel, N., Waitukaitis, S. & van Hecke, M. Jigsaw puzzle design of pluripotent origami. *Nat. Phys.* **16**, 63–68 (2020).
27. Overvelde, J. T. B., Weaver, J. C., Hoberman, C. & Bertoldi, K. Rational design of reconfigurable prismatic architected materials. *Nature* **541**, 347–352 (2017).
28. Lee, T.-U. et al. Self-locking and stiffening deployable tubular structures. *Proc. Natl. Acad. Sci. USA* **121**, e2409062121 (2024).
29. Tan, B. & Liu, K. Quantized energy absorption of sandwiched origami ring. *Extrem. Mech. Lett.* **70**, 102183 (2024).
30. Zhang, C. et al. Plug & play origami modules with all-purpose deformation modes. *Nat. Commun.* **14**, 4329 (2023).
31. Wu, S. et al. Stretchable origami robotic arm with omnidirectional bending and twisting. *Proc. Natl. Acad. Sci. USA* **118**, e2110023118 (2021).
32. Melancon, D., Forte, A. E., Kamp, L. M., Gorissen, B. & Bertoldi, K. Inflatable origami: multimodal deformation via multistability. *Adv. Funct. Mater.* **32**, 2201891 (2022).
33. Chen, P. et al. Design and fabrication of bistable actuators with high load capacity based on origami. *IEEE/ASME Trans. Mechatron.* **30**, 7019–7030 (2025).
34. Suzuki, H. & Wood, R. J. Origami-inspired miniature manipulator for teleoperated microsurgery. *Nat. Mach. Intell.* **2**, 437–446 (2020).
35. Han, M. et al. Submillimeter-scale multimaterial terrestrial robots. *Sci. Robot* **7**, eabn0602 (2022).
36. Melancon, D., Gorissen, B., García-Mora, C. J., Hoberman, C. & Bertoldi, K. Multistable inflatable origami structures at the metre scale. *Nature* **592**, 545–550 (2021).
37. Zhu, Y. & Filipov, E. T. Large-scale modular and uniformly thick origami-inspired adaptable and load-carrying structures. *Nat. Commun.* **15**, 2353 (2024).
38. Nelson, T. G., Zimmerman, T. K., Magleby, S. P., Lang, R. J. & Howell, L. L. Developable mechanisms on developable surfaces. *Sci. Robot* **4**, eaau5171 (2019).
39. Cai, J. et al. Compressive reusability of self-stable programmable assembled origami structures. *Int. J. Mech. Sci.* **310**, 111114 (2026).
40. Liu, K., Tachi, T. & Paulino, G. H. Invariant and smooth limit of discrete geometry folded from bistable origami leading to multistable metasurfaces. *Nat. Commun.* **10**, 4238 (2019).
41. Liu, K., Pratapa, P. P., Misseroni, D., Tachi, T. & Paulino, G. H. Triclinic metamaterials by tristable origami with reprogrammable frustration. *Adv. Mater.* **34**, 2107998 (2022).
42. Yin, Y. et al. A unified cut topology that endows programmable bistability in modular kirigami morphing structures. *Cell Rep. Phys. Sci.* **5**, 102335 (2024).
43. Dang, X., Chen, S., Acha, A. E., Wu, L. & Pasini, D. Shape and topology morphing of closed surfaces integrating origami and kirigami. *Sci. Adv.* **11**, eads5659 (2025).
44. Yoneda, T., Miyamoto, Y. & Wada, H. Structure, design, and mechanics of a pop-up origami with cuts. *Phys. Rev. Appl.* **17**, L021004 (2022).
45. ASTM D5470-17, “Standard Test Method for Thermal Transmission Properties of Thermally Conductive Electrical Insulation Materials,” (ASTM International, 2017).
46. Castelli, L., Zhu, Q., Shimokusu, T. J. & Wehmeyer, G. A three-terminal magnetic thermal transistor. *Nat. Commun.* **14**, 393 (2023).
47. Bao, N. et al. Gas-phase microactuation using kinetically controlled surface states of ultrathin catalytic sheets. *Proc. Natl. Acad. Sci. USA* **120**, e2221740120 (2023).
48. Liu, Q. et al. Electronically configurable microscopic metasheet robots. *Nat. Mater.* **24**, 109–115 (2025).
49. Miao, R., Kishore, R., Kaur, S., Prasher, R. & Dames, C. A non-volatile thermal switch for building energy savings. *Cell Rep. Phys. Sci.* **3**, 100960 (2022).
50. Yang, T. et al. Millimeter-scale liquid metal droplet thermal switch. *Appl. Phys. Lett.* **112** (2018).

51. Du, T. et al. Wide range continuously tunable and fast thermal switching based on compressible graphene composite foams. *Nat. Commun.* **12**, 4915 (2021).
52. Hu, P. et al. Hyperelastic Kevlar nanofiber aerogels as robust thermal switches for smart thermal management. *Adv. Mater.* **35**, 2207638 (2023).
53. Feng, H. et al. Thermally-responsive hydrogels Poly(N-isopropylacrylamide) as the thermal switch. *J. Phys. Chem. C.* **123**, 31003–31010 (2019).
54. Kommandur, S. & Kishore, R. A. Contact-based passive thermal switch with a high rectification ratio. *ACS Eng. Au* **3**, 76–83 (2023).
55. Wang, J. et al. Rapid temperature-responsive thermal regulator for safety management of battery modules. *Nat. Energy* **9**, 939–946 (2024).
56. Castelli, L. et al. A thermal regulator using passive all-magnetic actuation. *Cell Rep. Phys. Sci.* **4**, 101556 (2023).
57. Sood, A. et al. An electrochemical thermal transistor. *Nat. Commun.* **9**, 4510 (2018).
58. Terakado, N., Nara, Y., Machida, Y., Takahashi, Y. & Fujiwara, T. Dynamic control of heat flow using a spin-chain ladder cuprate film and an ionic liquid. *Sci. Rep.-Uk* **10**, 14468 (2020).
59. Yang, Q. et al. Solid-state electrochemical thermal transistors. *Adv. Funct. Mater.* **33**, 2214939 (2023).
60. Hartquist, C. M. et al. Reversible two-way tuning of thermal conductivity in an end-linked star-shaped thermoset. *Nat. Commun.* **15**, 5590 (2024).

## Acknowledgements

We thank Ms. Yiwei Hu for helpful discussions regarding the visualizations in this article. We acknowledge Prof. Quanshui Zheng for generously sharing the lab facilities for high-vacuum thermal test. This work was supported by the National Natural Science Foundation of China (grants 12372159, 52450136, 52521007, and 52476045), the National Key Research and Development Program of China (grants 2022YFB4701900 and 2024YFB4405700).

## Author contributions

Conceptualization: K.L., L.Y. Methodology: K.L., L.Y., B.T., J.L., B.S. Investigation: B.T., J.L., F.Y., K.X., S.Q., L.Y., K.L. Visualization: B.T., J.L., K.X. Funding acquisition: K.L., L.Y. Project administration: K.L., L.Y. Supervision: K.L., L.Y. Writing – original draft: B.T., J.L. Writing – review & editing: K.L., L.Y.

## Competing interests

The authors declare no competing interests.

## Additional information

**Supplementary information** The online version contains supplementary material available at <https://doi.org/10.1038/s41467-026-69956-2>.

**Correspondence** and requests for materials should be addressed to Lin Yang or Ke Liu.

**Peer review information** *Nature Communications* thanks Xudong Zhang and the other anonymous reviewer(s) for their contribution to the peer review of this work. A peer review file is available.

**Reprints and permissions information** is available at <http://www.nature.com/reprints>

**Publisher's note** Springer Nature remains neutral with regard to jurisdictional claims in published maps and institutional affiliations.

**Open Access** This article is licensed under a Creative Commons Attribution-NonCommercial-NoDerivatives 4.0 International License, which permits any non-commercial use, sharing, distribution and reproduction in any medium or format, as long as you give appropriate credit to the original author(s) and the source, provide a link to the Creative Commons licence, and indicate if you modified the licensed material. You do not have permission under this licence to share adapted material derived from this article or parts of it. The images or other third party material in this article are included in the article's Creative Commons licence, unless indicated otherwise in a credit line to the material. If material is not included in the article's Creative Commons licence and your intended use is not permitted by statutory regulation or exceeds the permitted use, you will need to obtain permission directly from the copyright holder. To view a copy of this licence, visit <http://creativecommons.org/licenses/by-nc-nd/4.0/>.

© The Author(s) 2026